



# Impacts of Muddy Bed Aggregates on Sediment Transport and Management in the Tidal James River, VA

David W. Perkey<sup>1</sup>; S. Jarrell Smith, Ph.D., P.E., M.ASCE<sup>2</sup>; Kelsey A. Fall<sup>3</sup>; Grace M. Massey, Ph.D.<sup>4</sup>; Carl T. Friedrichs, Ph.D., Aff.M.ASCE<sup>5</sup>; and Emmalynn M. Hicks<sup>6</sup>

**Abstract:** Aggregation state significantly influences the size, density, and transport characteristics of fine sediment. Understanding sediment transport and deposition processes in the nation's navigable waterways is a primary mission for the US Army Corps of Engineers (USACE), particularly when it comes to infilling of navigation channels. In this study, a newly developed camera system was used to evaluate the aggregation state of eroded sediment from cores collected in the tidal James River, VA. Results showed that bed sediments were composed mostly of mud, but that erosion predominately occurred in the form of aggregates with median sizes 50–270 times larger than the disaggregated sediment. Aggregate size weakly correlated to shear stress at levels <2 Pa, as well as sand content and bed density. A numerical simulation demonstrated that mud aggregates were predicted to transport in incipient suspension or bedload, while disaggregated fines were predominately maintained in full suspension. This difference in transport mode has significant implication for channel infilling and sediment transport within the system. **DOI: 10.1061/(ASCE)WW.1943-5460.0000578**. This work is made available under the terms of the Creative Commons Attribution 4.0 International license, http://creativecommons.org/licenses/by/4.0/.

#### Introduction

Sediment aggregates are composed of smaller particles bound by the cohesive forces of clay or organic material. They are formed by varying processes, resulting in different characteristics. Aggregates formed within the water column due to colliding cohesive sediments are commonly termed "flocs" (e.g., Mehta and McAnally 2008; Smith and Friedrichs 2011; Mehta 2013). Flocs are low-density aggregates with loose structures that are destroyed after deposition and burial in the sediment bed. Biological activity can also result in the formation of aggregated particles in the form of fecal pellets that vary in size and density with the species of generation (Edelvang and Austen 1997; Wright et al. 1997; Cutter and Diaz 2000; Schaffner et al. 2001; Forsberg et al. 2018). Another form of mud aggregate is that which results directly from erosion. When consolidated cohesive beds are eroded, the erosion often

<sup>1</sup>Engineer Research and Development Center-Coastal and Hydraulics Laboratory, US Army Corps of Engineers, Vicksburg, MS 39180 (corresponding author). ORCID: https://orcid.org/0000-0003-3062-4984. Email: david.perkey@usace.army.mil

<sup>2</sup>Engineer Research and Development Center-Coastal and Hydraulics Laboratory, US Army Corps of Engineers, Vicksburg, MS 39180. ORCID: https://orcid.org/0000-0002-8649-5598. Email: jarrell.smith@usace.army.mil

<sup>3</sup>Engineer Research and Development Center-Coastal and Hydraulics Laboratory, US Army Corps of Engineers, Vicksburg, MS 39180. Email: kelsey.a.fall@usace.army.mil

<sup>4</sup>Virginia Institute of Marine Science, William & Mary, Gloucester Point, VA 23062. Email: grace.massey@vims.edu

<sup>5</sup>Virginia Institute of Marine Science, William & Mary, Gloucester Point, VA 23062. ORCID: https://orcid.org/0000-0002-1810-900X. Email: carl.friedrichs@vims.edu

<sup>6</sup>Virginia Institute of Marine Science, William & Mary, Gloucester Point, VA 23062. Email: ehicks@vims.edu

Note. This manuscript was submitted on September 17, 2019; approved on January 6, 2020; published online on June 5, 2020. Discussion period open until November 5, 2020; separate discussions must be submitted for individual papers. This paper is part of the *Journal of Waterway, Port, Coastal, and Ocean Engineering*, © ASCE, ISSN 0733-950X.

occurs in the form of mud clasts, or bed aggregates, which have a particle density equal to that of the bed. Such action is previously described as mass erosion (e.g., Mehta and McAnally 2008; Winterwerp et al. 2012; Mehta 2013). This paper focuses mostly on the latter of the three types of aggregates, and the reader should assume that unless otherwise noted further reference to aggregated particles in this paper is to those of eroded bed aggregates.

The aggregation state of sediment can significantly impact the size and density of particles and thus alter the transport characteristics of sediments (Smith and Friedrichs 2011; Mehta 2013; Forsberg et al. 2018), which makes aggregates of significant interest to the management of sediment within ports, harbors, navigation channels, and coastal waterways. To maintain the nation's ports and channels, the USACE expends approximately \$1.4 billion annually and removes  $>1.4 \times 10^8 \,\mathrm{m}^3$  of material in dredging activities (USACE 2016). Discerning the sediment sources and conveyance mechanisms that lead to infilling is therefore a crucial component to effectively managing sediment within the nation's waterways. Numerical models are commonly utilized as tools to predict sediment movement. However, at present many of these numerical models (e.g., AdH, SEDZLJ, Delft3D, ROMS) either weakly describe or do not include aggregate properties and transport processes (Brown et al. 2019; Thanh et al. 2008; Lesser et al. 2004; Warner et al. 2008). In many applications, such as the placement of dredged material in channel-adjacent areas, the lack of aggregate transport process descriptions could result in very poor and misleading estimates of project performance and impact (Perkey and Smith 2019).

Numerous studies report the presence of mud aggregates both preserved in the lithological record and in modern deposits across a wide variety of environments. Terms such as "rip-up clasts" (e.g., Knight 1999; Fujiwara et al. 2000; Benito et al. 2003; Bondevik et al. 2003; Donnelly 2005; Goto et al. 2011), "mud balls" (e.g., Little 1982; Bachmann and Wang 2014); and "mud pebbles" (e.g., Karcz 1972; Durian et al. 2007) are commonly used to describe centimeter-sized mud aggregates associated with high-energy events such as floods, storms, and tsunamis. In addition, mud aggregates ranging in size from tens of microns to a few

millimeters are also observed in less-energetic environments (e.g., Rust and Nanson 1989; Wright and Marriott 2007; Plint et al. 2012; Gastaldo et al. 2013). Anthropogenic activities, such as dredging, have also been noted to produce aggregated clasts from the consolidated bed (e.g., Fettweis et al. 2009; Smith and Friedrichs 2011; Carey et al. 2013). The widespread documentation of these clasts of fine sediments speaks not only to their frequency of occurrence, but also to their durability through cycles of erosion, transport, and deposition following initial formation. Limited laboratory-based flume studies have been conducted in part to evaluate the transport processes and durability of mud aggregates (e.g., Smith 1972; Jepsen et al. 2010; Schieber et al. 2010). These studies note that aggregate durability varies with physical properties, such as mud and water content, but that transport distances on the order of tens of meters to many kilometers are possible under the right conditions. More commonly, recent research has focused on the erosion and transport processes of lower-density flocs (e.g., Pejrup and Mikkelsen 2010; Smith and Friedrichs 2011; Winterwerp et al. 2012; Forsberg et al. 2018). The examination of these same processes for higher-density bed aggregates remains largely unknown and undocumented in the scientific literature. Further, the impact that these aggregates might have on predictive sediment transport model outputs also remains a subject with little documentation.

The goal of this paper is to present sediment data that describe the presence and erosion of mud aggregates in an environment where frequent dredging and efficient sediment management practices are a concern, such as the tidal James River in Virginia. Present maintenance dredging practices within the system often involve channel-adjacent placement of dredged material, a process that calls for the disposal of dredged sediments in unconfined areas within a few hundred meters of the navigation channel. Of particular concern is the possibility that aggregated mud clasts transport primarily in bedload and spend less time in suspension than do the fine (<63 µm) particles that compose the aggregates. Such a difference in transport pathways could significantly alter the fate of fine sediments in the system. A novel approach was used to characterize

the size of particles mobilized from the bed with the Sedflume erosion device in conjunction with a newly developed camera system. The resulting size distributions of eroded material were evaluated to ascertain the aggregated state of the mobilized sediment. These data were used to illustrate the impact of aggregation state on sediment transport processes predicted by numerical methods within the vicinity of a frequently utilized dredged material placement area.

# **Study Site**

The tidally influenced portion of the James River, VA, encompasses the river downstream of Richmond, and has been described by Nichols et al. (1991) in three distinct morphologic zones: (1) the "meander zone" from Richmond downstream to Jordan Point, (2) the "funnel" from Jordan Point downstream to the river mouth at the entrance to the Chesapeake Bay, and (3) the "bay mouth" from the river mouth out to the Atlantic Ocean. The study area lies within the "funnel" reaches of the estuary, and stretches approximately 120 km from Jordan Point downstream to the river mouth (Fig. 1), hereafter referred to as the James River. Federally maintained navigation channels span this region of the river, which is underlain by sediment deposits consisting of upward-fining units composed of mixed gravel, sand, silt, and clay (Teifke and Onuschak 1973; Nichols et al. 1991). Prior surveys have observed that the bottom sediment varies spatially across the system, with mixtures of mud and fine sand common through the "funnel" (Nichols 1972; Nichols et al. 1991). Mean peak tidal currents at 1–2 m above the bed range between approximately 40 and 60 cm/s (Nichols et al. 1991). However, the highest velocities in the system are associated with river flood discharge events that produce velocities >280 cm/s in the "meander zone" just upstream of the study site, while storm events superimposed on tides produce currents on the order of 100 cm/s near the "bay mouth" portion of the estuary (just downstream of Fig. 1) (Nichols et al. 1991). Depths in the system typically range from 0.5 to 30 m,

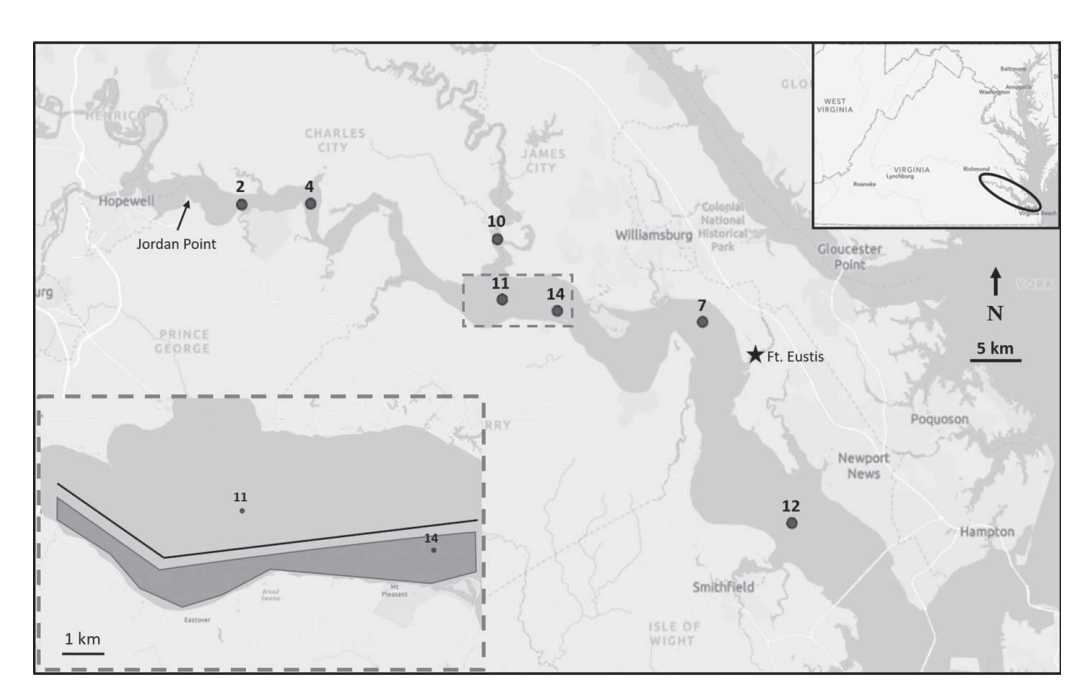


**Fig. 1.** The James River study area, with numbered dots indicating coring locations. The dashed box and insert shown with dashed lines indicate the Dancing Point–Swann Point numerical simulation area, with the navigation channel indicated with a solid line and the shaded region indicating the approximate location of dredged material disposal area. The mobile laboratory location at Fort Eustis Harbor is indicated with the star. (Map data from VITA, Esri, HERE, Garmin, SafeGraph, INCREMENT P, METI/NASA, USGS, EPA, NPS, US Census Bureau, USDA.)

with a reported mean (including lateral shoals) of 6 m (Nichols et al. 1991; Shen and Lin 2006).

It is estimated that 45%–92% of the river sediments being brought down the James River are deposited within the estuary (Nichols 1990). Accumulation rates vary across the estuary, with an average annual accumulation of 0.5 cm/yr, though rates as high as 11 cm/yr have been observed in portions of the estuary near the turbidity maxima and no-net current zones (Nichols 1972; Nichols et al. 1991). To maintain the federal channel, the USACE has had to perform routine maintenance dredging. As previously mentioned, many of these dredging projects place material in channel-adjacent disposal areas. From 2015 to 2018, dredging projects removed an average annual volume of 5.9 × 10<sup>5</sup> m<sup>3</sup> of sediment from the channel, at an average cost of approximately \$5 million per year (USACE 2019). During this period, dredging has frequently been required twice annually within the Dancing Point–Swann Point area (Fig. 1).

# Methodology

# Sample Collection

Sediment cores were collected with a  $34 \times 34 \times 61$  cm<sup>3</sup> stainless-steel box corer in November 2017. Upon recovery, each box core was subsampled with three, 10 cm-diameter polycarbonate tubes.

**Table 1.** Sediment core summary

Core	Latitude (° North)	Longitude (° West)	Collection date	Core type	Core length (cm)
2	37.3023	77.1609	11/9/2017	Box	19.5
4	37.30306	77.0855	11/8/2017	Box	18
7	37.20454	76.6567	11/7/2017	Box	31-32
10	37.27339	76.8812	11/8/2017	Box	16
11	37.22315	76.8759	11/8/2017	Box	33–35
12	37.03652	76.559	11/7/2017	Box	28-31
14	37.21366	76.8156	11/8/2017	Box	34–35

Two subcores were extruded at 1 cm intervals immediately upon collection and used for grain-size analysis. The other subcore was stored in an upright position following collection and transported by vessel to Fort Eustis Harbor, where erosion testing was performed. Table 1 provides core logging information, while the flow chart in Fig. 2 shows the testing and sampling performed on each of the collected cores.

# **Experimental Set-up**

To examine erosion processes associated with surface sediments within the study area, the data presented in this paper are limited to the upper 6 cm of each core. Erosion testing was performed with the USACE- developed Sedflume, which is a derivative of the flume developed by researchers at the University of California at Santa Barbara (McNeil et al. 1996). It is a field-deployable flume for quantifying cohesive sediment erosion over a wide range of shear stresses. A mobile laboratory housing the Sedflume was set up at the Fort Eustis Harbor (Fig. 1), where all erosion testing was performed. Cores were inserted into the Sedflume and a screw jack was used to advance the core so that the surface became flush with the bottom wall of the flume (Fig. 3). Site water was pumped into the flume and over the core surface, producing shear stress on the sample bed. As sediment was eroded from the core surface, the operator advanced the screw jack to maintain the sediment surface flush with the bottom wall of the erosion flume. Generally, erosion experiments were performed by repeating a sequence of increasing shear stresses that are determined by erosion rate measurements acquired during flume operation. Physical samples of the erosion surface were collected every 1-3 cm during erosion experiments to characterize grain size distribution through laser diffraction particle size analysis (LDPSA) techniques and bulk density [Fig. 3(a), Table 2]. This allowed for two sediment samples to be obtained within the upper 6 cm of erosion testing. A more detailed description of the Sedflume and its operational procedures are provided in McNeil et al. (1996).

To image and size the sediment particles resultant from erosion, the Flume Imaging Camera System (FICS) was attached to the

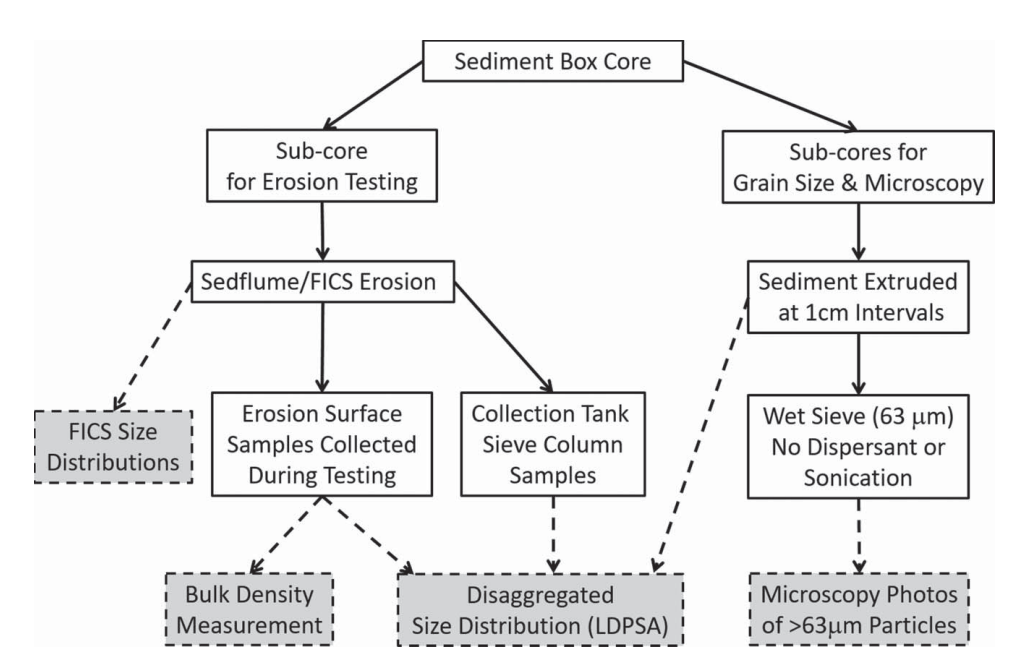


**Fig. 2.** Flow chart showing the testing and sampling sequence of sediment cores. Solid arrows and boxes indicate sample handling steps, while dashed arrows and shaded boxes indicate types of data collected. Multiple disaggregated size distributions were obtained from various sample types through laser diffraction techniques, while size distributions of eroded particles were obtained solely through video analysis.

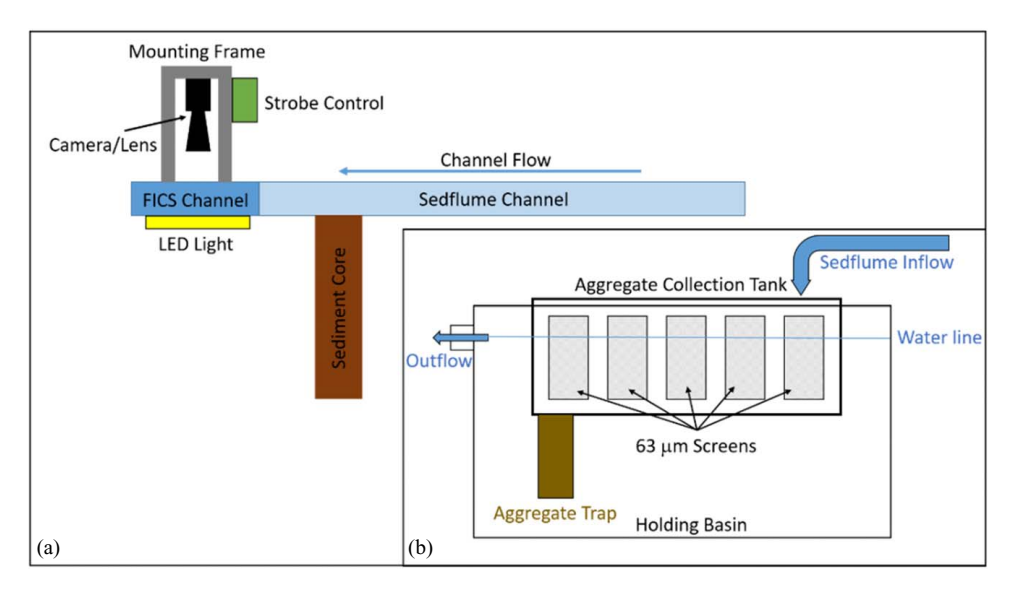


Fig. 3. (a) Schematic showing the flume imaging camera system (FICS) mounted to the outflow end of the Sedflume; and (b) the aggregate collection tank

**Table 2.** Physical properties of sediment samples

		S	Sedflume test bed	samples			Flume effluent samples			Extruded	Extruded grain size	
Core	Depth (cm)	% Fines (<63 μm)	D <sub>50L</sub> (μm)	D <sub>50F</sub> (μm)	FICS <i>n</i> (# particles)	ρ (g/cm <sup>3</sup> )	Depth (cm)	τ (Pa)	% Fines (<63 μm)	Depth (cm)	% Fines (<63 μm)	
2	1.2	21.3	172; 223 <sup>a</sup>	460	128,390	1.68	0.6	0.7	8.8	0–1	60.5	
2	4.5	78.9	25	1,680	1,008	1.57	4.3	3.5	39.2	4–5	35.2	
4	1.2	76.1	25	1,270	24,182	1.29	0.9	1.5	66.5	0-1	74.2	
4	5	73.0	32	3,410	8,308	1.33	3.7	3.0	63.6	3–4	65.1	
7	1.6	86.3	14	840	41,301	1.23	0.9	1.1	81.5	0-1	88.4	
7	5.8	91.6	12	1,990	15,870	1.28	4.1	4.1	93.4	3–4	89.0	
10	0.9	34.0	146; 212 <sup>a</sup>	290	25,026	1.74	0.6	0.7	13.7	0-1	19.1	
10	4.1	29.8	169; 219 <sup>a</sup>	270	39,502	1.64	3.2	0.7	1.2	3–4	26.0	
11	1.9	92.3	15	1,220	17,179	1.19	0.9	0.9	88.4	0-1	93.8	
11	5.5	87.3	16	4,960	3,182	1.21	4.8	2.6	90.9	4–5	91.4	
12	1.1	87.4	18	1,020	24,423	1.36	0.4	0.6	80.5	0-1	84.4	
12	5.7	91.5	12	3,310	10,146	1.31	4.6	3.2	89.5	4–5	83.3	
14	1.5	89.8	15	1,370	2,781	1.25	0.7	0.8	89.3	0-1	89.0	
14	4.7	90.7	15	1,940	2,841	1.23	3.9	1.6	91.0	3–4	90.6	

<sup>&</sup>lt;sup>a</sup>Indicates adjusted  $D_{50L}$  for sediments >66  $\mu$ m.

outflow end of the Sedflume [Fig. 3(a)]. The FICS consists of a clear polycarbonate channel, an Allied Vision camera equipped with a bi-telecentric lens, and an Allied Vision LED back light. The system is capable of sizing particles with equivalent spherical diameters (esd)  $\geq$ 66  $\mu$ m. Videos were collected with the FICS at every erosion interval, and an automated image analysis routine was used to generate a volume-based size distribution of particles recorded in the FICS videos. To compare the size of eroded particles with that of the particles in the sediment bed, FICS size distributions were matched with the grain size data obtained from the physical samples collected at the nearest depth from each erosion core (Table 2). Appendix I presents further details on the FICS equipment, setup, and processing routines.

As with sampling of the test bed, effluent from the Sedflume was captured with a collection tank twice within the upper 6 cm of erosion testing (Table 2). The collection tank is a 129 L acrylic tank with a series of 63  $\mu m$  screen windows along the side walls to

allow water and fine suspended sediment to pass through the system [Fig. 3(b)]. When in use, the tank is semi-emerged in water within a larger holding basin positioned under the outflow of the flume, approximately 2 m downstream of the erosion test bed. Material collected within the tank was swept to a submerged vertical settling column. Particles then settled through a series of 8 progressively finer sieves, ranging from 8,000 to 63 µm, and spaced at a  $1\phi$  interval. Effluent samples were collected during erosion tests at a specific flow over durations that typically ranged from 30 to 180 s and corresponded to 2-3 mm of recorded erosion. Material retained on each sieve was photographed (Fig. 4) to illustrate the size of eroded mud aggregates. Once photographed, contents of each sieve from the settling column were consolidated by rinsing with distilled water into 1 L bottles. Sediment within these bottles were then disaggregated and analyzed by LDPSA to evaluate the aggregation state of the eroded material retained on the sieves.

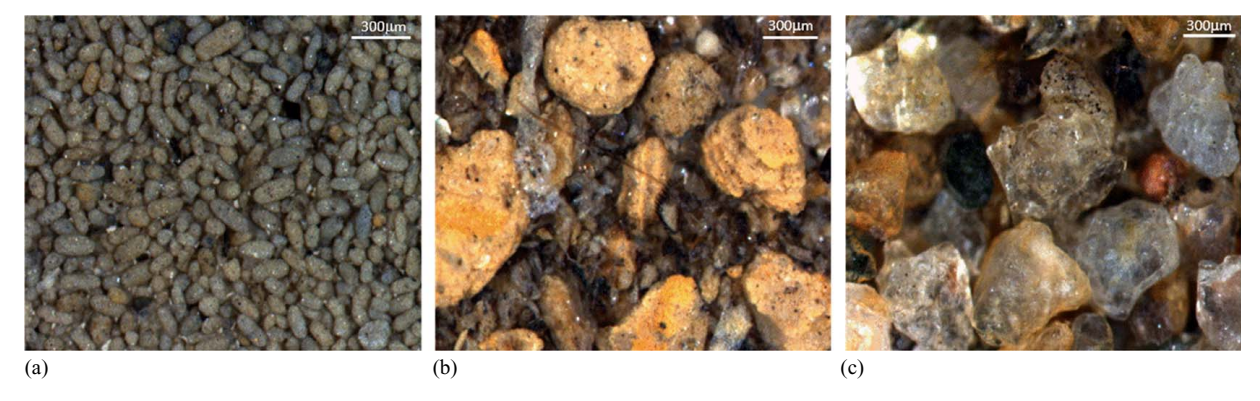


Fig. 4. Images collected under 30× magnification of nondispersed and nonsonicated sediment retained on 63 μm mesh: (a) Core 12 1–2 cm; (b) Core 14 3-4 cm; and (c) Core 2 3-4 cm.

## Sediment Characterization

## **Grain Size Analysis**

As shown in Fig. 2, grain size analysis was conducted on a variety of sediment samples collected in this study. Three techniques were used to compare particle size of sediments samples: LDPSA, FICS image analysis, and microscopy. Methods used for each technique are described here.

LDPSA. A Malvern Mastersizer 2000 laser diffraction particle-sizer was used to measure the particle-size distributions for all sediment samples. The Malvern measures particle size over the range 0.02– 2000 µm. Sediments were homogenized and disaggregated overnight in a solution of sodium metaphosphate (40 g/L). To remove macro organic material, samples were passed through a 1,000 µm sieve into the instrument's reservoir and sonicated for 60 s prior to analysis.

FICS Size Distributions. Prior to the start of erosion testing, background FICS videos of site water were recorded to account for any sediment particles present in the water not associated with bed erosion. To analyze the imaged particles, a total of 19 equal logarithmically spaced ( $\sim 1/3 \phi$ ) particle-size bins were generated that spanned the size range of 63-16,000 μm. These bin properties were used to generate a volume-based particle-size distribution for all the FICS videos. FICS distributions obtained from background videos were subtracted from videos recorded during erosion testing, to produce a net distribution representative of eroded particles. The number of particles in net distributions ranged from approximately 1,000 to 128,000 (Table 2).

Microscopy Imaging. To evaluate the presence of naturally occurring mud aggregates within the sediments collected from the James River, 30× magnification images were taken with a Nikon SMZ1000 model C-DSS115 dissecting microscope equipped with a Southern Microscope DR5 camera. An aliquot of each 1 cm-interval sediment sample extruded from the grain-size analysis cores was gently wet sieved with saline (15 ppt) water through a 63 µm mesh. Samples were not exposed to dispersant or sonication prior to sieving. Sediments retained on the sieve were transferred to Petri dishes and placed under the microscope for imaging.

#### **Bulk Density Measurements**

© ASCE

During erosion testing, physical samples were collected from the erosion surface to characterize the bulk sediment density of the test bed. Water content (w) of each sample was measured through wet-dry weight analysis following ASTM D2216-19 (ASTM 2019). The total volume of sample was assumed to consist of both solid particles and water, with assumed densities of 2.65 and 1.0 g/cm<sup>3</sup>, respectively. The bulk density as a function of w was calculated with Eq. (1) derived from Jepsen et al. (2010):

$$\rho = \rho_s + \frac{w\rho_s(\rho_w - \rho_s)}{\rho_w + w\rho_s} \tag{1}$$

## Numerical Estimation of Sediment Transport Type

Depth-averaged velocity and water-column height data obtained from the USACE Curvilinear Hydrodynamics 3D (CH3D) model were used to estimate theoretical transport modes of sediment in the vicinity of the Dancing Point-Swann Point dredged material placement area (Fig. 1). CH3D has been utilized previously in numerous studies to model the hydrodynamics of the Chesapeake Bay system, including the James River (e.g., Johnson et al. 1993; Cerco et al. 2002; Park et al. 2008). Model data from within the demonstration area were available for the time period April 1-9, 2000. Hydrodynamic data from this time period span across near-neap through spring tidal conditions, and river discharge levels near Richmond, VA, ranged between 150 and 270 m<sup>3</sup>/s (USGS 2019). Simulated maximum current speeds were ~50 cm/s and reflect those of typical tidal forcing similar to conditions during the November 2017 field sampling, but do not reflect conditions that may occur during river flooding or storm events (Nichols et al. 1991).

In this transport scenario, two sediment classifications were evaluated. The first classification simulated disaggregated grains of mud that ranged in size from 4 to 63 µm with a density of 2.65 g/cm<sup>3</sup>. The second sediment class represented bed aggregates ranging in size from 50 to 10,000 µm, a size range that roughly corresponds with aggregates observed in other studies that were previously discussed. Particle density of the bed aggregates was set to 1.25 g/cm<sup>3</sup> to match the measured bed density within the Swann Point-Dancing Point area (Table 2). Transport behavior was evaluated at particle diameters (D) at 100 equal logarithmically spaced intervals across the size range of each classification. It was assumed that initial mobilization of particles had already occurred and that, once mobilized, they behaved in a noncohesive manner. Continued transport of material was estimated by well-established relationships for transport of discrete sediment particles. The threshold of continued sediment motion was determined by the modified Shields criterion equation from Soulsby and Whitehouse (1997) and calculated for both types of particle densities. The particlesettling velocity was determined from the modified Stokes particle-settling relationship (Schiller and Naumann 1933), and transport modes were inferred from the balance of gravitational

settling and turbulent mixing, as expressed by the dimensionless Rouse number,  $P = w_s / \kappa u_*$ , where  $w_s$  is the settling velocity. Near-bed values of u(z),  $u_*$ , and  $\tau_b$  were estimated with CH3D data through law of the wall techniques for a z = 30 cm above the bed. In these calculations, it is important to note that two types of hydraulic roughness are utilized. When determining particle Rouse numbers, a hydraulic roughness representative of the turbulent mixing associated with the sediment bed roughness is appropriate. Therefore, based on values reported by Soulsby (1997), a total hydraulic roughness  $(z_{ot})$  for a mud/sand mixed-bed value of 0.7 mm was used in calculating  $u_*$ . In contrast, when evaluating  $\tau_b$ , the hydraulic roughness is in reference to skin friction with the particles in the bed, and the particle size was used to determine the skin friction hydraulic roughness ( $z_{os} = D/12$ ) and calculate the appropriate  $u_*$  (Soulsby 1997). In both instances, water temperature and salinity were assumed to be 10°C and 15 ppt, respectively.

Four states of mobility were evaluated for both populations. Particles were considered to remain mobile when either  $\tau_b \geq \tau_c$  or when the Rouse parameter predicted that turbulent mixing was adequate to maintain particles in suspension. When these conditions were not met particles were classified as immobile. Following the guidelines of van Rijn (1984), Rouse values were used to further classify mobile particles into three subgroups: (1) bedload, (2) incipient suspension, and (3) full suspension (Table 3).

#### Results

# **Grain Size & Aggregation State**

LDPSA results of the cores extruded for grain-size analysis showed that the cores were predominately composed of muddy sediment. Core 2 and Core 10 showed higher compositions of sand, but in general the James River sediments were found to be primarily composed of muddy sediment (Appendix II). These findings are consistent with other grain-size characterizations of the estuary sediments from previous sampling (Nichols 1972).

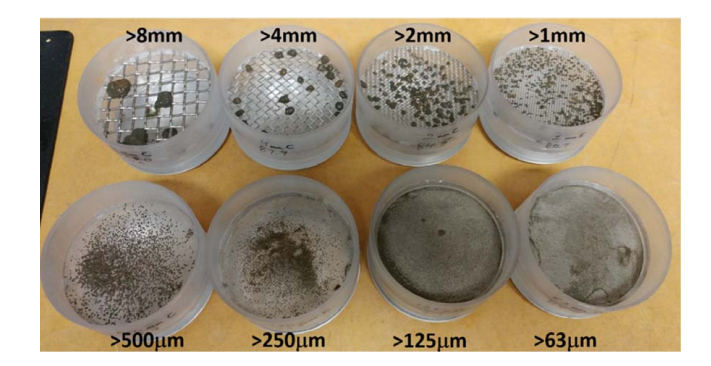
Images of the >63 µm wet sieved sediments placed under a microscope at 30× magnification provided visual evidence of aggregated clasts (Fig. 4). Prolate ellipsoid pellets on the order of 100-200 µm in length were commonly seen in many of the images [Fig. 4(a)]. The size and shape of these particles are similar to those previously reported as benthic fecal pellets in the James River (Moncure and Nichols 1968; Nichols 1972) and elsewhere (e.g., Taghon et al. 1984; Edelvang and Austen 1997; Schaffner et al. 2001; Patel and Desai 2009. Images also showed larger (>300 μm) and more-spherical aggregated clasts at lower frequency than the pellets [Fig. 4(b)]. LDPSA results from Core 14 sediment showed that mineral particles >300 µm accounted for less than 1% of the sample volume, and thus the clasts seen in Fig. 4(b) are almost certainly aggregated. The noncylindrical shape in conjunction with their irregular edges suggest that these aggregates are not biogenic in origin. These clasts may instead be due to direct rip-up from the sediment bed. Despite their origin, both types of aggregated particles are noticeably different in appearance than the mineral grains imaged in the sand rich sediments of Core 2 [Fig. 4(c)].

Table 3. Particle mobility classification parameters

Classification	Condition requirements
Immobile	$\tau_b \le \tau_c \& p > 2.5$
Mobile, bedload	$\tau_b \ge \tau_c \& p > 2.5$
Mobile, incipient suspension	$1$
Mobile, full suspension	$p \leq 1$

Sediment samples collected from the effluent of the Sedflume showed that muddy clasts were commonly produced as a result of bed erosion. Fig. 5 provides an example photograph of the material eroded from ~0.5 cm depth within Core 14 at 0.8 Pa. It can clearly be seen that sediment clasts ranging in size from several millimeters down to 63 µm were mobilized from the bed during erosion testing. The aggregation state of the retained material was evaluated by disaggregating the effluent sediment and analyzing the material by laser diffraction. Following disaggregation, the material pictured in Fig. 5 had a mud content (<63 µm) of 89%, indicating that nearly all the particles captured on the sieves were in an aggregated state. Similar results were observed for most of the effluent samples collected. Table 2 presents the depth, associated shear stress, and disaggregated percent fines for all the effluent samples collected. All but four of the samples were found to have fines contents greater than 60%, again indicating that the majority of sediments captured on the sieves were in an aggregated form. In addition, Table 2 presents the percent fines from the corresponding depth of the cores extruded for grain-size analysis and the test bed samples collected from the Sedflume cores. In most instances, the disaggregated fines content of the material captured on the sieves was within 10% of fines content for LDPSA samples at similar depths from both the Sedflume and extruded grain-size cores. The similarity in composition between the eroded material and that of the sediment bed suggests these aggregates are direct rip-up clasts from the bed, and that limited winnowing of fines was occurring during the erosion of the cohesive bed. It is worthwhile to point out that instances of fines content discrepancies >10% were limited to cores with the highest sand content, Cores 2 and 10. In these sandier cores, it is possible that fines were being winnowed from the bed as discrete particles and that aggregated mud clasts were less common.

FICS size distributions also documented the erosion of muddy clasts. To illustrate the distinct differences between grain size distributions obtained from eroded particles and the disaggregated bed, Fig. 6 presents the paired FICS and LDPSA size distributions from Core 14. The associated shear stress applied during the collection of these FICS distributions was 0.5 and 1.0 Pa for the upper and lower sample, respectively. LDPSA distributions (Fig. 6) showed a median grain size  $(D_{50L})$  of approximately 15 µm (Table 2) and less than 4% of the total volume was attributed to particles >100 μm. By comparison, 100% of the total measured particle volume was attributed to clasts >100 µm in the FICS distributions. FICS median grain sizes  $(D_{50F})$  from Core 14 were approximately 1,400 and 1,900 µm for the upper and lower samples, respectively (Table 2). These values are roughly 100 times greater than the corresponding disaggregated medians obtained through LDPSA (Table 2).



**Fig. 5.** Sediment retained on sieves following erosion of Core 14 0.5 cm depth at 0.8 Pa.

The distinct trends seen in Core 14 for FICS versus LDPSA results were consistently observed throughout most of the other cores (Table 2 and Appendix III).  $D_{50F}$  values ranged from 270 to 5,000  $\mu$ m while  $D_{50L}$  ranged from 15 to 170  $\mu$ m (Table 2). Differences in  $D_{50}$  values were larger in muddy sediment where  $D_{50F}$ values were on the order of 50–270 times larger than  $D_{50L}$ . Visual review of the FICS videos confirmed the presence of large aggregated clasts >1,000 µm moving through the flume following mobilization from the bed [Fig. 7(b)]. In contrast, the sandiest samples, namely the 0-2 cm sample from Core 2 and both the samples from Core 10, did not show nearly as large a disparity between the  $D_{50\mathrm{F}}$  and  $D_{50\mathrm{L}}$  (Table 2). Instead,  $D_{50\mathrm{F}}$  from these paired samples were less than 3 times greater than  $D_{50L}$  values and agreed within 300 µm of each other. LDPSA showed the sand contents of the eroded sediment from these depths to be greater than 65% (Table 2). In addition, grain-size data from the disaggregated effluent samples indicated >10% disparity in fines content with the eroded bed (Table 2). As previously mentioned, this may have been a result of winnowed fines from the bed at these depths. Because the FICS is not capable of sizing particles <66 µm, winnowed fines would bias the resultant distribution. To ensure that FICS and LDPSA distributions from the sandy samples were not distinct due to differences in their measurement capabilities, distributions using only sediment >66 µm were

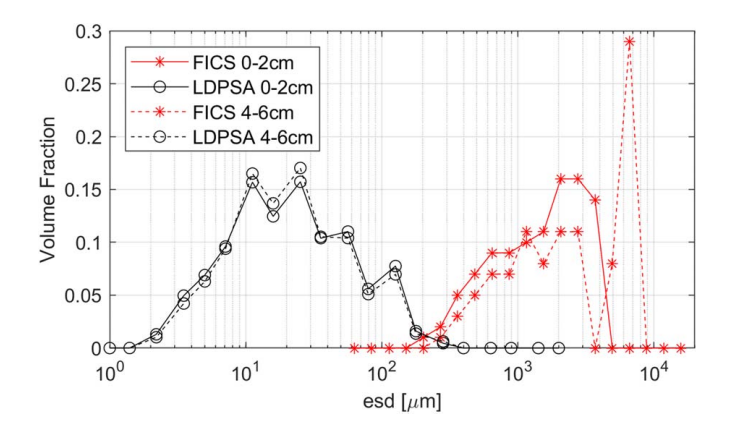


**Fig. 6.** Size distributions for Core 14. Plots with circles indicate disaggregated laser diffraction results from physical samples of eroded core, and plots with asterisks indicate results from flume videos collected at closest proximity to sampling depths. Depth of sample is denoted with line style.

compared. This reduced the difference between  $D_{50\mathrm{F}}$  and  $D_{50\mathrm{L}}$  to 1.2–2.0 times.

To evaluate if bed aggregate presence and size was a function of shear stress, correlations between  $D_{50F}$  and shear levels were examined. Muddy bed aggregates were consistently observed at shear stresses that ranged from approximately 0.1–8.5 Pa. The  $D_{50\rm F}$ were plotted against shear stress for all erosion intervals in all cores [Fig. 7(a)]. In examining the data across the entire range of applied shear stresses, a significant (<0.05) correlation (r) to  $D_{50F}$ was not observed ( $r^2 = 0.035$ , p = 0.07). The videos with  $D_{50F}$  values >5,500 µm were flagged as statistical outliers and were more closely examined to confirm the presence of large particles. Inspection of the FICS videos confirmed the presence of aggregated particles of this size [Fig. 7(b)] and therefore these data were not removed from the sample population. Visual examination of the data suggested that a stronger relationship between  $D_{50F}$  and shear stress might exist at lower levels of shear stress (≤2 Pa). When restricted to these lower-energy cases,  $r^2$  increased to approximately 0.17 [Fig. 7(c)]. While not a strong correlation, it was found to be statistically significant (p < 0.001) and indicates that at lower energy levels, aggregate size is weakly positively correlated to shear stress. However, during larger-energy events this relationship deteriorated and became statistically insignificant. This may be because the very largest stresses result in break-up of the largest aggregates.

FICS median grain-size values were also evaluated for correlations to sediment bed properties such, as sand content (>63 µm) and  $\rho$ . Values of these properties were obtained from the physical samples collected during Sedflume testing (Table 2) and used to generate linearly interpolated percentage sand and bed densities for each core. Sand content ranged from approximately 8% to 72%, while  $\rho$  ranged from approximately 1.2 to 1.7 g/cm<sup>3</sup>. Weak, but statistically significant negative correlations were observed for both sand ( $r^2 = 0.13$ , p = 0.003) and  $\rho$  ( $r^2 = 0.16$ , p = 0.001) in relation to  $D_{50F}$ . Further, it was observed that samples with higher bed density ( $\geq 1.6 \text{ g/cm}^3$ ) were also associated with sand content  $\geq 40\%$  (Fig. 8). A multiple linear regression model of both sand content and  $\rho$  did not account for additional variance in the  $D_{50F}$  data ( $r^2 = 0.16$ , p = 0.005). Multiple linear regression models that included shear stress in addition to sand and  $\rho$  were also evaluated. The incorporation of shear stress did not increase  $r^2$  values and was not found to be statistically significant, with p-values of 0.54 and 0.69 for regressions with sand and density, respectively. In general, the data from the James River cores

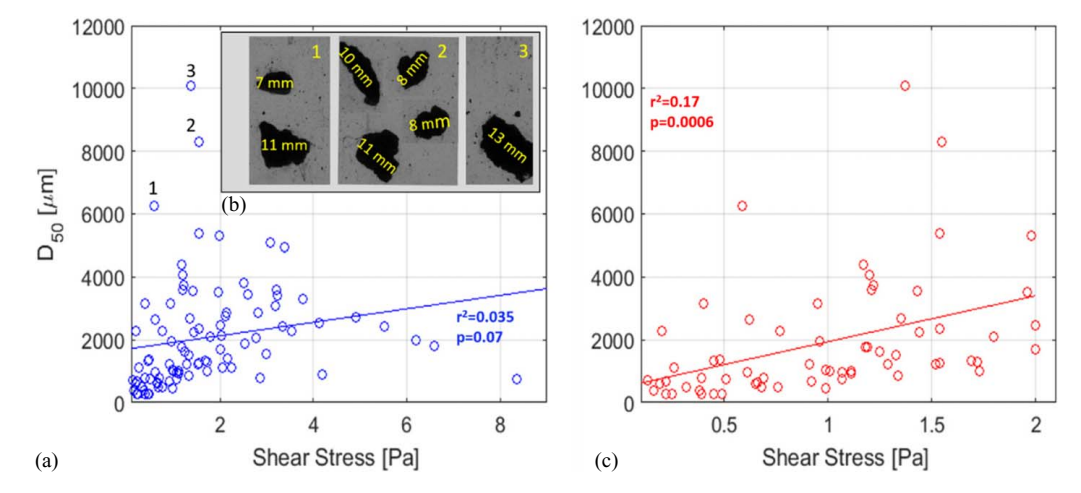


**Fig. 7.** (a) Compiled flume video  $D_{50}$  from all James River Estuary erosion tests plotted against shear stress; (b) with insert showing images of >5,500  $\mu$ m esd aggregates from outlier  $D_{50}$  samples; and (c) the  $D_{50}$  plotted against shear up to 2 Pa.

indicated that larger mud aggregates produced during erosion were derived from sediment beds with a lower sand and higher water content, and that shear stress had a limited impact on aggregate size at levels ≤2 Pa.

# **Numerical Simulation of Transport**

The distinct differences in sediment transport modes of disaggregated silt-sized particles and aggregated mud clasts were evaluated for the Dancing Point-Swann Point area of the James River and are presented in Fig. 9. The figure plots the fraction of time over the nine-day scenario that particles were either actively transported in full suspension, incipient suspension (having intermittent contact with the bed), or bedload, or were immobile on the bed. Fig. 9(a) depicts transport behavior of disaggregated silt-size particles with a density of 2.65 g cm<sup>-3</sup>. This particle description best matches that obtained through LDPSA measurements. These sediments were shown to be maintained in full suspension throughout much of the scenario, with only coarser silts having limited periods of immobility for less than 10% of the time. Settling velocities for this class of particle never produced a Rouse value >2.5, and thus they were never predicted to be transported in bedload.

In contrast to the transport behavior of silt particles, Fig. 9(b) presents transport behavior that would be expected for aggregated

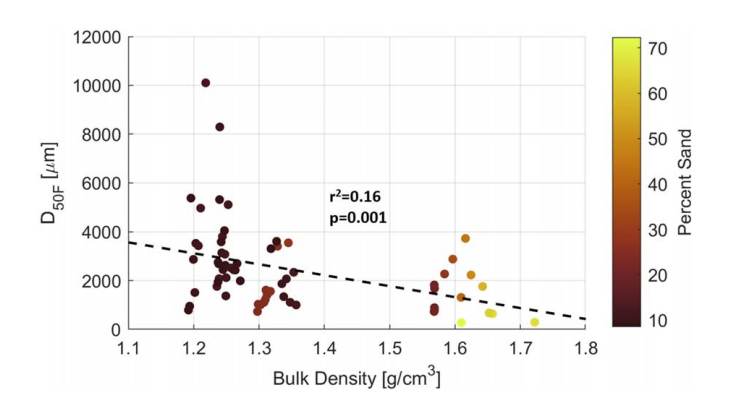


**Fig. 8.** Compiled flume video  $D_{50}$  from all James River erosion tests plotted against bulk density. A best-fit linear regression is indicated with a dashed line and associated  $r^2$  and p-values of the fit are provided in the figure. Symbol shading corresponds to the sand content of the sediment bed.

mud clasts similar to those observed with the FICS and retained on the sieves during erosion testing. As previously described, this class of particle ranged in size from 50 to 10,000 µm, with a density of 1.25 g cm<sup>-3</sup>. Mud aggregates in the 50–180 μm size range remained in full suspension more than 80% of the time, a similar result to that of the disaggregated silt particles. However, as aggregate size increased beyond 180 µm, transport behavior significantly deviated from that of disaggregated particles. An aggregate 400 µm in size was no longer maintained in full suspension, but instead was estimated to move in incipient suspension 66% of the time and as bedload 12% of the simulation. As aggregate size increased beyond 750 µm, the transport pathway was limited to only bedload. This size aggregate was commonly observed on the sieves following erosion testing and within the FICS videos. It is important to point out that erosion testing of the mud-dominant sediment beds produced  $D_{50F}$  values >750 µm.

#### **Discussion and Conclusions**

Testing conducted on sediment cores collected from the James River Estuary consistently showed evidence that erosion of the sediment bed occurred in the form of aggregated mud clasts. Visual observations described erosional processes that occurred both as "plucking," as well as larger bed failure events. These erosion behaviors are commonly referred to as "surface erosion" and "mass erosion," respectively (e.g., Mehta and McAnally 2008; Winterwerp et al. 2012; Mehta 2013). Surface-erosion processes in muddy beds have typically been associated with the remobilization of recently deposited, unconsolidated, low-density flocs (e.g., Thomsen and Gust 2000; Schieber et al. 2010; Mehta 2013; Forsberg et al. 2018). Conversely, mass-erosion processes are more commonly associated with stiff and highly consolidated beds (Mehta 2013). The characteristics of the cores and eroded material in this study contrast these generalizations. Muddy cores from the James River Estuary had densities that predominately ranged between 1.2 and 1.4 g/cm<sup>3</sup> (Fig. 8), indicating that they were moderately to weakly consolidated, and comparable with beds formed from deposition in other estuaries (Mehta 2013). However, surface "plucking" erosion of these sediments occurred as clasts of the consolidated bed, not as recently deposited flocs. In addition, aggregates resulting from bed failure and mass erosion events were observed in these same, relatively weak, moderately to wellconsolidated beds.

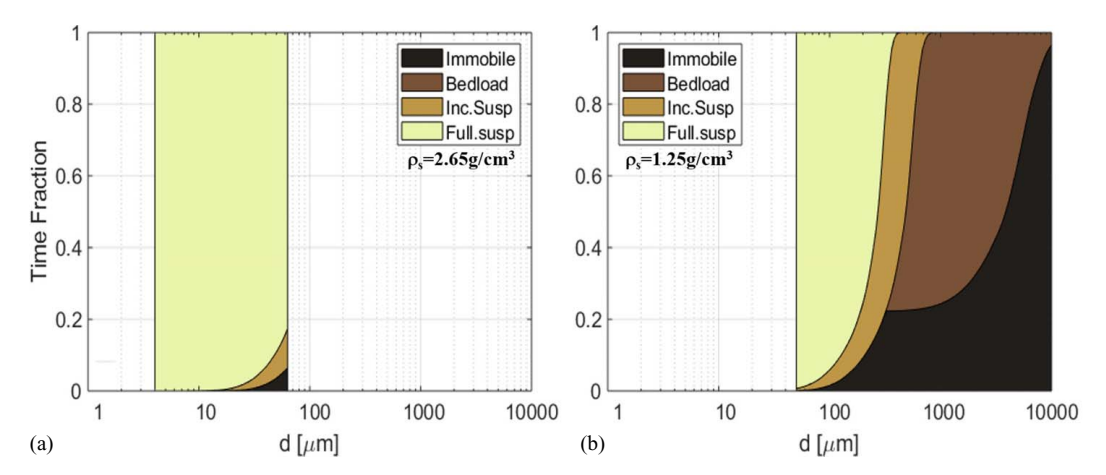


Fig. 9. Estimates of transport mode by particle size for muddy sediments at Dancing Point–Swann Point for (a) primary mineral; and (b) mud aggregate particles.

Recognition of these types of aggregates is largely missing from the engineering and scientific literature, as well as the numerical models used to simulate sediment transport in estuarine and coastal environments. In this study, muddy bed aggregates, ranging in size from a few hundred microns to several millimeters, were produced and survived transport across a wide range of shear stresses (0.1– 8 Pa) (Fig. 7). While most of the larger bed aggregates (>4,000 μm) were observed when shear stress was ≤2 Pa, mud clasts >1,000 µm were observed at shear stresses as high as 6.5 Pa (Fig. 7). This distinguishes them from similarly sized flocs, which have limited strength and durability and tend to break apart in higher energy-flow conditions (e.g., Hunt 1986; McCave and Hall 2006; Forsberg et al. 2018). This suggests that aggregates derived from moderately to well-consolidated beds are capable of surviving transport in more-energetic conditions than are flocs. Further, the density of aggregates produced from consolidated beds is expected to be higher than that of recently deposited flocs. In turn, bed aggregate-settling velocities would be higher than equivalently sized flocs, reducing time in suspension and favoring transport by bedload versus by suspension.

Microscopy photographs of sediment collected across the study area further supported the observations of aggregated clasts within the system. Sand-sized, spherically shaped mud clasts [Fig. 4(b)] along with fecal pellets [Fig. 4(a)] were seen in multiple cores. The rounded edges and spherical nature of many of these clasts indicated physical weathering and abrasion from bedload transport within the estuary. Though the durability of these aggregates is uncertain, studies examining the lithological record in numerous environments have identified sand-sized aggregated mud clasts that were transported in bedload prior to deposition, burial, and lithification (e.g., Rust and Nanson 1989; Wright and Marriott 2007; Plint et al. 2012; Gastaldo et al. 2013). This suggests that the observations in this study are not isolated or unique to the James River Estuary. Further, while bed aggregates have frequently been associated with high-energy events (e.g., Knight 1999; Fujiwara et al. 2000; Benito et al. 2003; Bondevik et al. 2003; Donnelly 2005; Goto et al. 2011; Little 1982; Bachmann and Wang 2014; Karcz 1972; Durian et al. 2007), data from this study demonstrate that high-energy conditions are not required to erode and transport bed aggregates. Aggregated clasts were mobilized at shear stresses <1 Pa, suggesting that their production and transport may be common within the estuary, and not limited to intermittent, high-energy events.

Frequent mobilization of aggregated bed clasts from the sediment bed could significantly alter predicted sediment transport within coastal and estuarine environments. Numerical simulations conducted in this study indicated that these aggregates are transported differently than their constituent primary particles (Fig. 9). In contrast to fines, bed aggregates were more frequently transported by bedload, rather than suspension. Bedload transport of fine sediment is currently not included in commonly used sediment transport models (e.g., AdH, SEDZLJ, Delft3D, ROMS), and therefore are not represented in their outputs (Brown et al. 2019; Thanh et al. 2008; Lesser et al. 2004; Warner et al. 2008). These aggregated bed clasts also had larger periods of immobility when compared with the predicted transport processes of silt-sized particles, increasing their residence time within the estuary. Such differences in transport processes will impact numerical model predictions, which influence sediment-management practices within coastal and estuarine environments.

Specific to this study, sediment management within the James River Estuary frequently calls for the placement of dredged material in areas within 500 m of the navigation channel. Previous research has found mud aggregates to be associated with

dredging-related activities (e.g., Fettweis et al. 2009; Smith and Friedrichs 2011; Carey et al. 2013). Because these aggregates are predicted to have limited mobility, largely restricted to bedload transport within the system, a likely fate for deposition is the nearby channel. Therefore, these aggregates could significantly influence management issues, such as channel infilling rates and life expectancies of placement areas. The presence of these types of bed aggregates is also expected outside of dredge-material placement sites. Previous studies conducted within the James River Estuary documented that mud aggregates composed approximately 20% of the sand-sized fraction in the upper estuary, and their abundance throughout the entire system was on the order of 5% (Nichols 1972). Erosion testing performed on muddy sediment cores throughout the estuary in this study did not show spatial limitation of bed aggregate production, however results did indicate that aggregate production was limited in sandy areas of the estuary. Bed aggregate production is, therefore, likely to occur throughout much of the muddy "funnel" portion of the estuary. The transport of muddy sediment clasts in bedload could significantly alter the fate of fine sediment, as deposition centers for bedload versus suspended load have been documented to differ across the estuary (Nichols et al. 1991). This difference in fine-sediment transport processes could be expected in similar muddy estuarine systems and, thus, results of previously conducted sediment transport models that did not account for the transport of fine sediment in bedload may inadequately represent the fate of fine sediment within their domain.

These points raise the need for the possible incorporation of bed aggregate clasts into sediment transport models. However, before this can be done, a better understanding of the physical characteristics of these clasts is needed. Data from this study indicated that size and abundance of these clasts were negatively correlated with bed density and sand content. Limited laboratory studies (e.g., Smith 1972; Jepsen et al. 2010; Schieber et al. 2010) have documented similar results and reported aggregate transport distances that varied from tens of meters to many kilometers, based on density and fines content. While these observations might be intuitive, further research is needed to define and constrain aggregate production, transport, and break-up rates. Although evidence of their abundance can be found in the lithological record (e.g., Rust and Nanson 1989; Wright and Marriott 2007; Plint et al. 2012; Gastaldo et al. 2013), information describing the physical properties of bed aggregates will be needed to not only characterize them for model incorporation, but govern when it is appropriate to include them in numerical simulations. In this system, the practice of channel-adjacent placement of dredged material is utilized, so the incorporation of bed aggregates into numerical simulations may be important because a likely fate for deposition of aggregates (when mobilized) is in the nearby channel. Conversely, in instances where bed aggregates quickly break apart or if near-field, shortterm transport processes are less of a concern, the need to represent bed aggregates in numerical simulations would be diminished and of little value.

# **Future Work**

Work is currently underway to incorporate the aggregate properties observed in this study into sediment-transport modeling being done with the USACE Geophysical Scale Transport Modeling System in the James River. While initial studies are occurring on the James River, the goal of this work is to demonstrate the potential importance of bed aggregate processes in similar mud-dominant locations across the country. To do so, research is being conducted

that examines the relationships between physical properties commonly associated with cohesion (e.g., clay content, bulk density, organic content, plasticity) and the production of bed aggregates. Further research is also being conducted that evaluates the durability of aggregates in conjunction with these same physical properties. The goal of this work is to provide a first-order understanding of when muddy aggregates are likely to occur and to determine their resilience and likely transport capabilities. This information can then be utilized to govern when and how these bed aggregates should be incorporated into numerical sediment transport models.

# Appendix I. Flume Imaging Camera System (FICS)

The FICS is a USACE Engineer Research and Development Center (ERDC)-developed system designed to characterize grain size distributions of sediment particles immediately following mobilization from the bed [Fig. 3(a)]. The FICS consists of a clear polycarbonate channel, an Allied Vision, Manta G504B (2,452 × 2,056 resolution, 3.45 μm<sup>2</sup> pixels, 2/3' image sensor) camera equipped with an Opto Engineering TC23056 bi-telecentric lens, and an Allied Vision LED back light paired with a Pulsar 320 strobe controller. The FICS channel is designed to attach directly to the outflow end of the Sedflume. It measures 22.5 cm in length and has the same  $2 \times 10$  cm cross-sectional area as the Sedflume channel. The camera and lens are centrally mounted 12.8 cm above the top of the channel. FICS images an area of  $4.5 \times$ 5.3 cm, with a focal depth of 2.7 cm. Magnification of the system is 0.157×, resulting in a subject pixel size of ~22 μm. Videos in this study were collected at a rate of 5 fps, with an exposure of 500 µs and gain set to 10. The backlight was pulsed with 24 V, 50 A with a pulse width of 30 µs. FICS videos had a default length of 240 frames (80 s) and were collected at every erosion interval. In cases where the erosion interval duration was <80 s, video collection was terminated early. For longer erosion intervals (duration >5 min), multiple videos were collected approximately every 5 min.

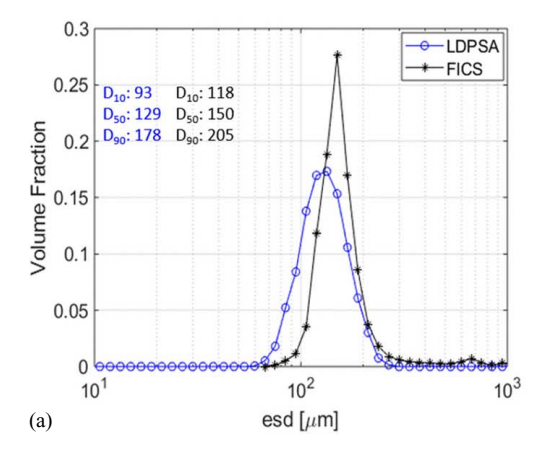
An automated image-analysis routine was used to characterize the size of eroded particles in FICS images. Prior to erosion testing, a calibration grid was inserted into the FICS channel and photographed for the purpose of transforming pixel space to length. The processing routine utilizes this gridded image and employs algorithms from the MATLAB Image Processing Toolbox. It combines local intensity thresholding with particle vetting to accurately

identify particles, while omitting unwanted features, such as background objects, air bubbles, and out-of-focus particles. FICS image processing requires particles to appear in an area of at least  $3\times3$  pixels. Therefore, the system can only accurately size particles with equivalent spherical diameters (esd) greater than approximately  $66~\mu m$ . Further details on these processing techniques can be found in Smith and Friedrichs (2011).

To evaluate the FICS particle-sizing routines, QA/QC testing with two sand types of known size range have been tested. Sieving techniques were used to generate (1) a very fine sand (63–125 μm) and (2) a very fine to coarse sand (63–1,000 μm). Volume-based distributions of both sands were obtained through LDPSA for comparison with FICS data. Results showed that both methods produced distributions that sized particles beyond the upper bounds of the sieve distribution (Fig. 10). Previous studies have documented coarser distribution results in LDPSA results when compared with sieve data (e.g., Konert and Vandenberghe 1997; Blott and Pye 2006). This is not surprising, as sieve data are based on the minimum particle axis, whereas LDPSA methods report a distribution based on equivalent spherical diameter (esd). FICS also reports results based on a calculated esd from a 2D projected area and, thus, some level of disparity in distribution data is to be expected between these techniques and sieves. A direct comparison between the FICS and LDPSA data showed that, in general, the size distributions were similar for both types of sand evaluated (Fig. 10). FICS distributions were consistently found to be slightly coarser, with  $D_{10}$ ,  $D_{50}$ , and  $D_{90}$  values being consistently 1.2–1.5 times larger than LDPSA values (Fig. 10). Review of FICS images showed periodic clumping of sand grains within the flume that likely contributed to a coarser distribution data generated by the FICS. In addition, a direct 1:1 relationship of FICS data to LDPSA data should not be expected, as the two methods use different techniques for sizing particles. Prior studies have shown that image analysis often results in coarser, narrower distributions compared with LDPSA (Xu and Di Guida 2003; Li et al. 2005). These data do, however, indicate that distributions obtained by the FICS are comparable with those obtained through LDPSA methods.

# Appendix II. Extruded-Core Grain Size Data

This appendix presents data obtained from the extruded sediment cores collected specifically for the purpose of grain-size characterization of the sediment bed. All data presented was obtained through laser diffraction particle size analysis (LDPSA) methods.



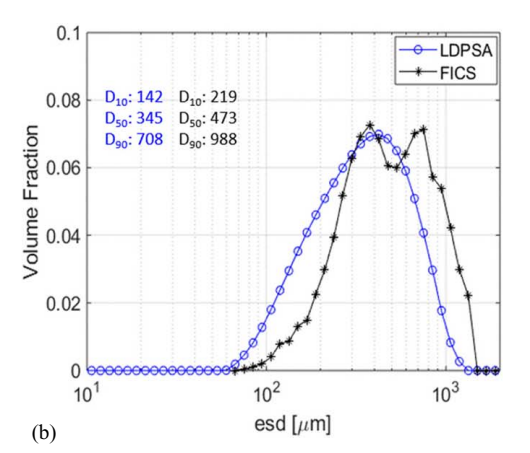


Fig. 10. Comparison of FICS and LDPSA size distributions of the two test sands: (a) very fine sand (63–125  $\mu$ m); and (b) very fine to coarse sand (63–1,000  $\mu$ m).

Data from each core is presented sequentially by identification number.

## Core 2

Fig. 11 shows the LDPSA grain-size distribution curves from the sediment samples extruded from the upper 6 cm of Core 2, while Table 4 presents the percent sand, silt, and clay along with the  $D_{10}$ ,  $D_{50}$ , and  $D_{90}$  values of those same samples.

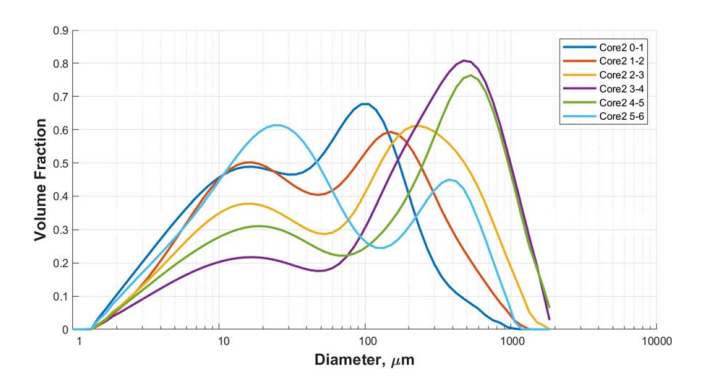


Fig. 11. Grain size distributions for Core 2 0–6 cm samples.

**Table 4.** Physical sample properties, Core 2

Sample #	Depth (cm)	D <sub>10</sub> (μm)	D <sub>50</sub> (μm)	D <sub>90</sub> (μm)	% Sand	% Silt	% Clay
1	0–1	5	40	192	40.0	53.4	6.6
2	1-2	7	51	316	46.4	49.4	4.2
3	2-3	7	105	558	58.0	37.8	4.2
4	3–4	10	255	885	74.6	22.5	2.9
5	4–5	8	209	874	65.0	31.3	3.8
6	5–6	6	36	433	38.1	56.3	5.6

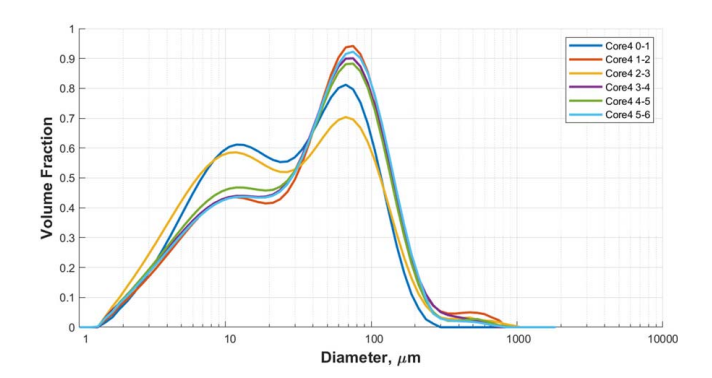


Fig. 12. Grain size distributions for Core 4 0–6 cm samples.

Table 5. Physical sample properties, Core 4

Sample #	Depth (cm)	D <sub>10</sub> (μm)	D <sub>50</sub> (μm)	D <sub>90</sub> (μm)	% Sand	% Silt	% Clay
1	0-1	5	28	103	26.5	67.8	5.7
2	1-2	6	44	133	37.6	57.0	5.5
3	2-3	5	26	114	27.2	65.0	7.9
4	3-4	5	41	129	35.6	58.2	6.2
5	4-5	5	38	124	34.2	59.5	6.3
6	5–6	5	42	128	36.3	57.7	6.0

#### Core 4

Fig. 12 shows the LDPSA grain-size distribution curves from the sediment samples extruded from the upper 6 cm of Core 4, while Table 5 presents the percent sand, silt, and clay along with the  $D_{10}$ ,  $D_{50}$ , and  $D_{90}$  values of those same samples.

## Core 7

Fig. 13 shows the LDPSA grain-size distribution curves from the sediment samples extruded from the upper 6 cm of Core 7, while

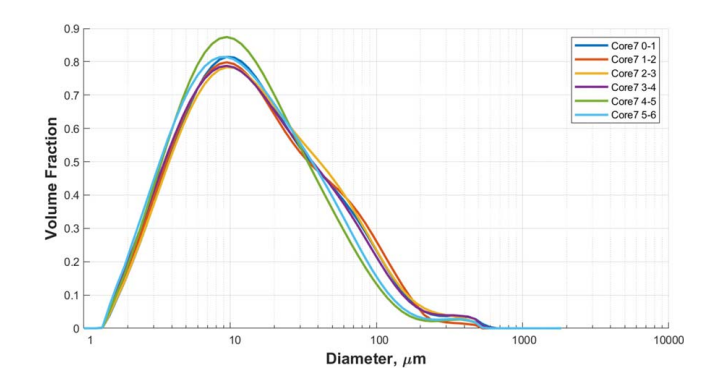
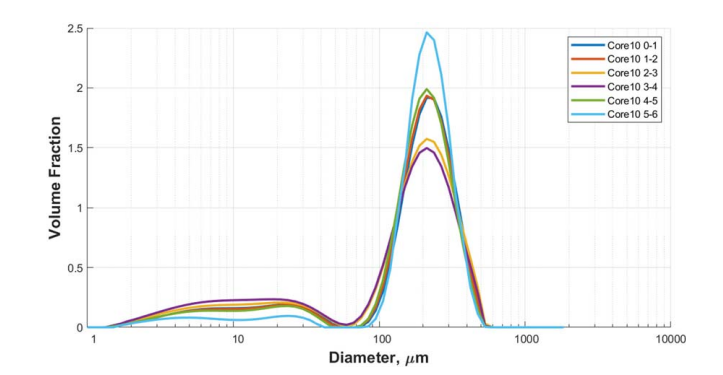


Fig. 13. Grain size distributions for Core 7 0–6 cm samples.

**Table 6.** Physical sample properties, Core 7

Sample #	Depth (cm)	D <sub>10</sub> (μm)	D <sub>50</sub> (μm)	D <sub>90</sub> (μm)	% Sand	% Silt	% Clay
1	0-1	4	13	70	12.0	76.4	11.6
2	1-2	4	13	71	12.2	75.3	12.4
3	2-3	4	14	71	12.3	76.1	11.7
4	3–4	3	13	68	11.3	75.5	13.1
5	4-5	3	12	50	7.2	79.5	13.4
6	5–6	3	12	55	8.3	77.4	14.3



**Fig. 14.** Grain size distributions for Core 10 0–6 cm samples.

**Table 7.** Physical sample properties, Core 10

Sample #	Depth (cm)	D <sub>10</sub> (μm)	D <sub>50</sub> (μm)	D <sub>90</sub> (μm)	% Sand	% Silt	% Clay
1	0–1	12	197	341	80.9	16.6	2.6
2	1-2	13	194	335	81.4	16.0	2.6
3	2-3	10	180	346	77.5	19.2	3.4
4	3–4	8	169	336	74.0	22.1	3.9
5	4–5	14	191	326	82.7	14.6	2.6
6	5–6	103	209	326	90.7	7.3	2.0

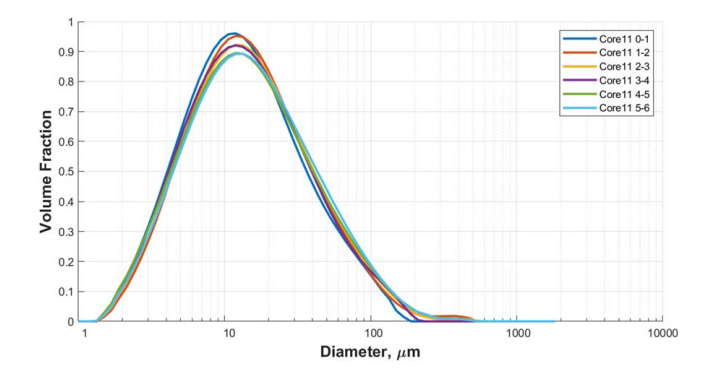


**Fig. 15.** Grain size distributions for Core 11 0–6 cm samples.

**Table 8.** Physical sample properties, Core 11

Sample #	Depth (cm)	D <sub>10</sub> (μm)	D <sub>50</sub> (μm)	D <sub>90</sub> (μm)	% Sand	% Silt	% Clay
1	0–1	4	14	54	7.9	84.0	8.0
2	1-2	4	14	56	8.3	83.0	8.7
3	2-3	4	13	53	7.6	83.1	9.4
4	3–4	4	14	57	8.9	81.6	9.5
5	4-5	4	14	59	9.2	82.1	8.7
6	5–6	4	14	54	7.9	84.0	8.0

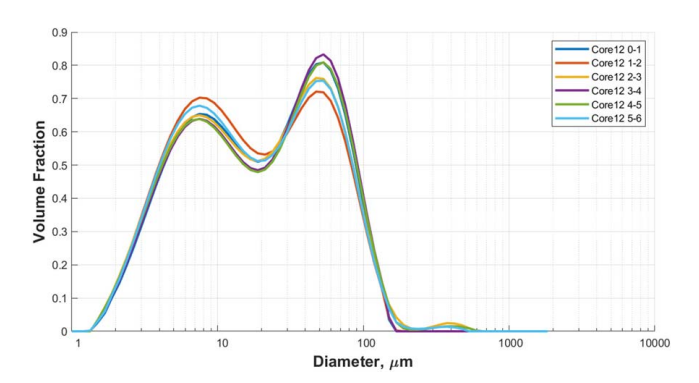


Fig. 16. Grain size distributions for Core 12 0-6 cm samples.

Table 9. Physical sample properties, Core 12

Sample #	Depth (cm)	D <sub>10</sub> (μm)	D <sub>50</sub> (μm)	D <sub>90</sub> (μm)	% Sand	% Silt	% Clay
1	0-1	4	20	76	16.2	74.2	9.6
2	1-2	4	17	73	14.4	75.0	10.6
3	2-3	4	19	77	16.2	73.2	10.5
4	3–4	4	20	77	17.1	73.1	9.9
5	4-5	4	20	79	17.4	72.3	10.3
6	5–6	4	18	76	15.6	74.0	10.3

Table 6 presents the percent sand, silt, and clay along with the  $D_{10}$ ,  $D_{50}$ , and  $D_{90}$  values of those same samples.

# Core 10

Fig. 14 shows the LDPSA grain-size distribution curves from the sediment samples extruded from the upper 6 cm of Core 10, while Table 7 presents the percent sand, silt, and clay along with the  $D_{10}$ ,  $D_{50}$ , and  $D_{90}$  values of those same samples.

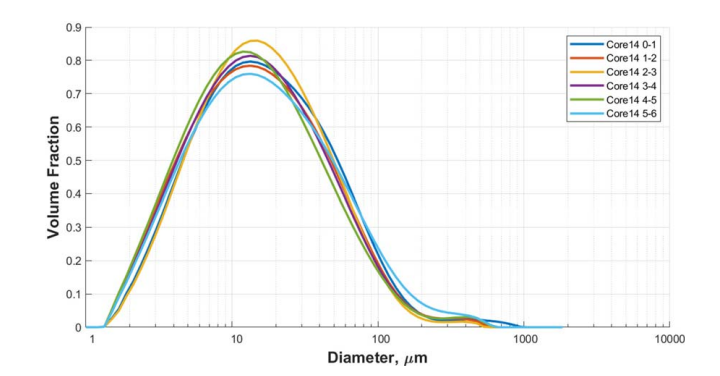


**Fig. 17.** Grain size distributions for Core 14 0–6 cm samples.

Table 10. Physical sample properties, Core 14

Sample #	Depth (cm)	D <sub>10</sub> (μm)	D <sub>50</sub> (μm)	D <sub>90</sub> (μm)	% Sand	% Silt	% Clay
1	0-1	4	16	67	11.4	79.7	8.9
2	1-2	4	15	62	10.0	78.6	11.4
3	2-3	4	15	59	9.0	82.4	8.5
4	3–4	4	14	61	9.7	79.4	10.9
5	4-5	4	14	58	9.1	79.1	11.8
6	5–6	4	16	74	12.9	76.5	10.6

#### Core 11

Fig. 15 shows the LDPSA grain-size distribution curves from the sediment samples extruded from the upper 6 cm of Core 11, while Table 8 presents the percent sand, silt, and clay along with the  $D_{10}$ ,  $D_{50}$ , and  $D_{90}$  values of those same samples.

## Core 12

Fig. 16 shows the LDPSA grain-size distribution curves from the sediment samples extruded from the upper 6 cm of Core 12, while Table 9 presents the percent sand, silt, and clay along with the  $D_{10}$ ,  $D_{50}$ , and  $D_{90}$  values of those same samples.

#### Core 14

Fig. 17 shows the LDPSA grain-size distribution curves from the sediment samples extruded from the upper 6 cm of Core 14, while Table 10 presents the percent sand, silt, and clay along with the  $D_{10}$ ,  $D_{50}$ , and  $D_{90}$  values of those same samples.

## Appendix III. Erosion-Testing Grain Size Data

This appendix presents grain size data obtained from the sediment cores eroded with the Sedflume. Data from each core is presented sequentially by identification number. For each core, laser diffraction particle size analysis (LDPSA) obtained from physical samples collected in the upper 6 cm is presented first, followed by data obtained with the FICS.

# Core 2

Table 11 presents the depth of physical samples collected from Core 2 within the upper 6 cm and their  $D_{10}$ ,  $D_{50}$ , and  $D_{90}$  values determined through LDPSA methods. By comparison, Table 12

presents the depth and  $D_{10}$ ,  $D_{50}$ , and  $D_{90}$  values of eroded particles measured by the FICS within the upper 6 cm of Core 2.

#### Core 4

Table 13 presents the depth of physical samples collected from Core 4 within the upper 6 cm and their  $D_{10}$ ,  $D_{50}$ , and  $D_{90}$  values determined through LDPSA methods. By comparison, Table 14 presents the depth and  $D_{10}$ ,  $D_{50}$ , and  $D_{90}$  values of eroded particles measured by the FICS within the upper 6 cm of Core 4.

Table 11. LDPSA physical sample properties, Core 2

Sample #	Depth (cm)	$D_{10}$ ( $\mu$ m)	$D_{50}$ ( $\mu$ m)	$D_{90}  (\mu { m m})$
1	1.2	17	173	563
2	4.5	6	25	116

**Table 12.** FICS distribution properties, Core 2

Sample #	Depth (cm)	D <sub>10</sub> (μm)	D <sub>50</sub> (μm)	D <sub>90</sub> (μm)
Core2_d01	0	220	680	2,060
Core2_d02	0.2	230	780	2,900
Core2_d03	0.4	210	500	1,280
Core2_d04	0.8	210	460	2,390
Core2_d05	1.9	210	640	2,510
Core2_d06	2.1	230	670	2,180
Core2_d07	24	390	1,760	4,810
Core2_d08	2.9	440	2,230	7,510
Core2_d09	3.1	440	3,730	7,890
Core2_d10	3.3	400	1,310	6,850
Core2_d11	3.7	580	2,880	7,690
Core2_d12	4.1	470	2,270	5,360
Core2_d13	4.8	410	1,680	3,230
Core2_d14	4.9	360	800	2,840
Core2_d15	5.1	360	890	2,330
Core2_d16	5.4	390	1,820	4,300
Core2_d17	5.8	320	730	2,140

Table 13. LDPSA physical sample properties, Core 4

Sample #	Depth (cm)	$D_{10}$ ( $\mu m$ )	$D_{50}$ ( $\mu m$ )	$D_{90}$ ( $\mu$ m)
1	1.2	6	25	102
2	5.0	6	32	102

Table 14. FICS distribution properties, Core 4

Sample #	Depth (cm)	$D_{10}$ ( $\mu$ m)	$D_{50}$ ( $\mu m$ )	$D_{90} (\mu m)$
Core4 d01	0	260	700	2,590
Core4 d02	0.1	160	280	860
Core4 d03	0.2	240	620	1,640
Core4 d04	0.4	380	930	2,100
Core4 d05	0.7	410	1,270	6,720
Core4 d06	1.6	350	730	1,450
Core4 d07	1.7	360	1,030	3,720
Core4 d08	2.1	370	1,010	2,910
Core4 d09	2.5	380	1,110	2,520
Core4 d10	2.7	410	1,220	3,190
Core4 d11	2.8	500	1,610	3,970
Core4 d12	3.0	430	1,410	3,390
Core4 d13	3.4	500	1,560	4,390
Core4 d14	4.4	720	3,410	10,510
Core4 d15	5.7	870	3,550	9,850
Core4 d16	6.0	620	2,240	5,310

#### Core 7

Table 15 presents the depth of physical samples collected from Core 7 within the upper 6 cm and their  $D_{10}$ ,  $D_{50}$ , and  $D_{90}$  values determined through LDPSA methods. By comparison, Table 16 presents the depth and  $D_{10}$ ,  $D_{50}$ , and  $D_{90}$  values of eroded particles measured by the FICS within the upper 6 cm of Core 7.

#### Core 10

Table 17 presents the depth of physical samples collected from Core 10 within the upper 6 cm and their  $D_{10}$ ,  $D_{50}$ , and  $D_{90}$  values determined through LDPSA methods. By comparison, Table 18 presents the depth and  $D_{10}$ ,  $D_{50}$ , and  $D_{90}$  values of eroded particles measured by the FICS within the upper 6 cm of Core 10.

#### Core 11

Table 19 presents the depth of physical samples collected from Core 11 within the upper 6 cm and their  $D_{10}$ ,  $D_{50}$ , and  $D_{90}$  values determined through LDPSA methods. By comparison, Table 20

**Table 15.** LDPSA physical sample properties, Core 7

Sample #	Depth (cm)	$D_{10}$ ( $\mu$ m)	$D_{50}$ ( $\mu m$ )	$D_{90}  (\mu {\rm m})$
1	1.6	4	14	76
2	5.8	4	12	55

**Table 16.** FICS distribution properties, Core 7

Sample #	Depth (cm)	$D_{10}$ ( $\mu$ m)	$D_{50}$ ( $\mu$ m)	$D_{90}  (\mu {\rm m})$
Core7 d01	0	150	270	950
Core7 d02	0.1	160	270	810
Core7 d03	0.5	200	480	1,200
Core7 d04	0.8	290	740	2,740
Core7 d05	1.3	330	840	2,480
Core7 d06	2.0	410	1,760	7,690
Core7 d07	2.3	440	2,080	5,500
Core7 d08	2.8	800	3,810	10,590
Core7 d09	3.1	600	3,080	7,220
Core7 d10	3.3	550	2,120	4,250
Core7 d11	3.6	980	5,100	11,090
Core7 d12	4.0	570	2,520	5,870
Core7 d13	4.3	560	2,440	5,020
Core7 d14	4.5	590	2,430	5,880
Core7 d15	4.8	550	2,700	8,320
Core7 d16	5.2	470	1,990	6,910

**Table 17.** LDPSA physical sample properties, Core 10

Sample #	Depth (cm)	$D_{10}$ ( $\mu$ m)	$D_{50}$ ( $\mu$ m)	$D_{90} (\mu m)$
1	0.9	9	147	352
2	4.1	9	169	352

**Table 18.** FICS distribution properties, Core 10

Sample #	Depth (cm)	$D_{10}$ ( $\mu$ m)	$D_{50}  (\mu {\rm m})$	D <sub>90</sub> (μm)
Core10 d01	0	870	2,280	2,660
Core10 d02	0.1	220	370	1,200
Core10 d05	1.5	190	290	550
Core10 d11	4.9	170	270	910

**Table 19.** LDPSA physical sample properties, Core 11

Sample #	Depth (cm)	$D_{10}$ ( $\mu$ m)	$D_{50}  (\mu { m m})$	D <sub>90</sub> (μm)
1	0.9	5	15	54
2	4.1	4	16	73

Table 20. FICS distribution properties, Core 11

Sample #	Depth (cm)	$D_{10}$ ( $\mu$ m)	$D_{50}$ ( $\mu$ m)	D <sub>90</sub> (μm)
Corel1 d01	0	230	610	1,640
Corel1 d02	0.2	320	1,110	4,430
Core11 d03	0.4	400	1,320	4,870
Corel1 d04	0.8	390	1,240	5,290
Corel1 d05	1.2	380	1,220	5,670
Corel1 d06	2.5	330	790	2,120
Corel1 d07	2.7	340	950	3,550
Core11 d08	3.0	530	5,370	12,760
Corel1 d09	3.5	590	2,870	7,610
Corel1 d10	3.8	780	1,510	2,290
Corel1 d11	4.0	890	3,530	5,920
Corel1 d12	4.6	940	3,430	6,610
Corel1 d13	5.0	1,190	4,960	8,030
Core11 d14	5.9	2,120	10,100	14,480

Table 21. LDPSA physical sample properties, Core 12

Sample #	Depth (cm)	$D_{10}$ ( $\mu$ m)	$D_{50}$ ( $\mu$ m)	$D_{90} (\mu m)$
1	1.1	4	18	68
2	5.7	4	12	57

Table 22. FICS distribution properties, Core 12

Sample #	Depth (cm)	$D_{10}$ ( $\mu$ m)	$D_{50}$ ( $\mu m$ )	$D_{90}  (\mu {\rm m})$
Core12 d01	0	190	380	750
Core12 d02	0.1	210	510	1,210
Core12 d03	0.2	310	980	3,480
Core12 d04	0.6	350	1,020	2,350
Core12 d05	1.7	340	1,000	2,790
Core12 d06	2.1	460	2,340	9,320
Core12 d07	2.5	370	1,110	3,610
Core12 d08	3.0	500	2,070	6,600
Core12 d09	3.4	390	1,340	2,990
Core12 d10	3.6	460	1,870	4,650
Core12 d11	4.3	800	3,610	9,100
Core12 d12	5.1	790	3,310	7,620

presents the depth and  $D_{10}$ ,  $D_{50}$ , and  $D_{90}$  values of eroded particles measured by the FICS within the upper 6 cm of Core 11.

## Core 12

Table 21 presents the depth of physical samples collected from Core 12 within the upper 6 cm and their  $D_{10}$ ,  $D_{50}$ , and  $D_{90}$  values determined through LDPSA methods. By comparison, Table 22 presents the depth and  $D_{10}$ ,  $D_{50}$ , and  $D_{90}$  values of eroded particles measured by the FICS within the upper 6 cm of Core 12.

# Core 14

Table 23 presents the depth of physical samples collected from Core 14 within the upper 6 cm and their  $D_{10}$ ,  $D_{50}$ , and  $D_{90}$  values determined through LDPSA methods. By comparison, Table 24 presents the depth and  $D_{10}$ ,  $D_{50}$ , and  $D_{90}$  values of eroded particles measured by the FICS within the upper 6 cm of Core 14.

Table 23. LDPSA physical sample properties, Core 14

Sample #	Depth (cm)	$D_{10}$ ( $\mu$ m)	$D_{50}$ ( $\mu$ m)	$D_{90}  (\mu {\rm m})$
1	1.5	4	15	63
2	4.7	5	15	59

**Table 24.** FICS distribution properties, Core 14

Sample #	Depth (cm)	D <sub>10</sub> (μm)	D <sub>50</sub> (μm)	D <sub>90</sub> (μm)
Core14 d01	0	580	3,150	7,500
Core14 d02	0.2	730	6,250	13,710
Core14 d03	0.5	550	2,290	5,690
Core14 d04	0.9	800	4,400	12,890
Core14 d05	1.9	370	1,370	3,290
Core14 d06	2.0	480	2,630	6,760
Core14 d07	2.3	640	4,050	11,350
Core14 d08	2.8	530	2,450	6,340
Core14 d09	3.1	600	3,140	6,760
Core14 d10	3.3	500	3,590	6,930
Core14 d11	3.7	1,110	8,290	14,030
Core14 d12	4.2	650	2,750	11,170
Core14 d13	5.4	520	1940	6,640
Core14 d14	5.6	540	2,690	6,670
Core14 d15	6.0	1,140	5,310	12,850

# **Data Availability Statement**

Some or all data, models, or code that support the findings of this study are available from the corresponding author, upon reasonable request. These data include .mat and .xlsx files containing grain-size distributions from both processed videos and physical samples, as well as bulk density and water content values obtained from sediment samples.

#### **Acknowledgments**

This work was jointly funded and supported by the Dredging Operations Environmental Research (DOER) Program, the Regional Sediment Management (RSM) Program, and the USACE Norfolk District Office (NAO). The authors would like to acknowledge assistance and support provided with both field logistics and laboratory analysis from T. W. Kirklin, J. M. Kirklin, R. S. Pruhs, the VIMS-CHSD Laboratory, and the US Army Fort Eustis Harbor. The involvement of C. T. Friedrichs was supported by NSF Grant OCE-1459708. This is Contribution No. 3884 of the Virginia Institute of Marine Science, William & Mary.

# References

ASTM. 2019. Standard test methods for laboratory determination of water (moisture) content of soil and rock by mass. ASTM D2216-19. West Conshohocken, PA: ASTM.

Bachmann, G. H., and Y. Wang. 2014. "Armoured mud balls as a result of ephemeral fluvial flood in a humid climate: Modern example from Guizhou Province, South China." J. Palaeogeogr. 3 (4): 410–418. https://doi.org/10.3724/SP.J.1261.2014.00064.

Benito, G., Y. Sánchez-Moya, and A. Sopeña. 2003. "Sedimentology of high-stage flood deposits of the Tagus River, Central Spain." *Sediment. Geol.* 157 (1–2): 107–132. https://doi.org/10.1016/S0037-0738(02)00196-3.

Blott, S. J., and K. Pye. 2006. "Particle size distribution analysis of sandsized particles by laser diffraction: An experimental investigation of

- instrument sensitivity and the effects of particle shape." *Sedimentology* 53 (3): 671–685. https://doi.org/10.1111/j.1365-3091.2006.00786.x.
- Bondevik, S., J. Mangerud, S. Dawson, A. Dawson, and Ø Lohne. 2003. "Record-breaking height for 8000-year-old tsunami in the North Atlantic." *Eos Trans. Am. Geophys. Union* 84 (31): 289–293. https://doi.org/10.1029/2003EO310001.
- Brown, G. L., J. N. McAlpin, K. C. Pevey, P. V. Luong, C. R. Price, and
  B. A. Kleiss. 2019. Mississippi River Hydrodynamic and Delta Management Study: Delta Management Modeling. AdH/SEDLIB Multi-Dimensional Model Validation and Scenario Analysis. Report.
  No. ERDC/CHL-TR-19-2. Engineer Research and Development Center Vicksburg Ms Vicksburg.
- Carey, D. A., K. Hickey, J. D. Germano, L. B. Read, and M. E. Esten. 2013. Monitoring survey at the Massachusetts Bay disposal site September/October 2013. DAMOS Contribution No. 195. Concord, MA: USACE.
- Cerco, C. F., L. Linker, J. Sweeney, G. Shenk, and A. J. Butt. 2002. "Nutrient and solids controls in Virginia's Chesapeake Bay tributaries." J. Water Resour. Plann. Manage. 128 (3): 179–189. https://doi.org/10.1061/(ASCE)0733-9496(2002)128:3(179).
- Cutter, Jr., G. R., and R. J. Diaz. 2000. "Biological alteration of physically structured flood deposits on the Eel margin, northern California." Cont. Shelf Res. 20 (3): 235–253. https://doi.org/10.1016/S0278-4343(99) 00059-X.
- Donnelly, J. P. 2005. "Evidence of past intense tropical cyclones from backbarrier salt pond sediments: A case study from Isla de Culebrita, Puerto Rico, USA." J. Coastal Res. 42: 201–210.
- Durian, D. J., H. Bideaud, P. Duringer, A. P. Schröder, and C. M. Marques. 2007. "Shape and erosion of pebbles." *Phys. Rev. E* 75 (2): 1–9. https://doi.org/10.1103/PhysRevE.75.021301.
- Edelvang, K., and I. Austen. 1997. "The temporal variation of flocs and fecal pellets in a tidal channel." *Estuarine Coastal Shelf Sci.* 44 (3): 361–367. https://doi.org/10.1006/ecss.1996.0149.
- Fettweis, M., J. S. Houziaux, I. Du Four, V. Van Lancker, C. Baeteman, M. Mathys, D. Van den Eynde, F. Francken, and S. Wartel. 2009. "Long-term influence of maritime access works on the distribution of cohesive sediments: Analysis of historical and recent data from the Belgian nearshore area (southern North Sea)." *Geo-Mar. Lett.* 29 (5): 321–330. https://doi.org/10.1007/s00367-009-0161-7.
- Forsberg, P. L., K. H. Skinnebach, M. Becker, V. B. Ernstsen, A. Kroon, and T. J. Andersen. 2018. "The influence of aggregation on cohesive sediment erosion and settling." *Cont. Shelf Res.* 171: 52–62. https://doi.org/10.1016/j.csr.2018.10.005.
- Fujiwara, O., F. Masuda, T. Sakai, T. Irizuki, and K. Fuse. 2000. "Tsunami deposits in Holocene bay mud in southern Kanto region, Pacific coast of central Japan." Sediment. Geol. 135 (1–4): 219–230. https://doi.org/10.1016/S0037-0738(00)00073-7.
- Gastaldo, R. A., B. A. Pludow, and J. Neveling. 2013. "Mud aggregates from the Katberg Formation, South Africa: additional evidence for Early Triassic degradational landscapes." J. Sediment. Res. 83 (7): 531–540. https://doi.org/10.2110/jsr.2013.45.
- Goto, K., et al.et al. 2011. "New insights of tsunami hazard from the 2011 Tohoku-oki event." *Mar. Geol.* 290 (1–4): 46–50. https://doi.org/10.1016/j.margeo.2011.10.004.
- Hunt, J. R., 1986. Particle aggregate breakup by fluid shear. In *Estuarine cohesive sediment dynamics*, 85–109. New York: Springer.
- Jepsen, R., J. Roberts, and J. Gailani. 2010. "Effects of bed load and suspended load on separation of sands and fines in mixed sediment." *J. Waterw. Port Coastal Ocean Eng.* 136 (6): 319–326. https://doi.org/10.1061/(ASCE)WW.1943-5460.0000054.
- Johnson, B. H., K. W. Kim, R. E. Heath, B. B. Hsieh, and H. L. Butler. 1993. "Validation of three-dimensional hydrodynamic model of Chesapeake Bay." J. Hydraul. Eng. 119 (1): 2–20. https://doi.org/10 .1061/(ASCE)0733-9429(1993)119:1(2).
- Karcz, I. 1972. "Sedimentary structures formed by flash floods in southern Israel." Sediment. Geol. 7 (3): 161–182. https://doi.org/10.1016/0037 -0738(72)90001-2.
- Knight, J. 1999. "Morphology and palaeoenvironmental interpretation of deformed soft-sediment clasts: Examples from within Late Pleistocene glacial outwash, Tempo Valley, Northern Ireland."

- *Sediment. Geol.* 128 (3–4): 293–306. https://doi.org/10.1016/S0037 -0738(99)00080-9.
- Konert, M., and J. E. F. Vandenberghe. 1997. "Comparison of laser grain size analysis with pipette and sieve analysis: A solution for the underestimation of the clay fraction." *Sedimentology* 44 (3): 523–535. https:// doi.org/10.1046/j.1365-3091.1997.d01-38.x.
- Lesser, G. R., J. A. Roelvink, J. A. T. M. van Kester, and G. S. Stelling. 2004. "Development and validation of a three-dimensional morphological model." *Coastal Eng.* 51 (8–9): 883–915. https://doi.org/10.1016/j .coastaleng.2004.07.014.
- Li, M., D. Wilkinson, and K. Patchigolia. 2005. "Comparison of particle size distributions measured using different techniques." Part. Sci. Technol. 23 (3): 265–284. https://doi.org/10.1080 /02726350590955912.
- Little, R. D. 1982. "Lithified armored mud balls of the Lower Jurassic Turners Falls sandstone, north-central Massachusetts." *J. Geol.* 90 (2): 203–207. https://doi.org/10.1086/628665.
- McCave, I. N., and I. R. Hall. 2006. "Size sorting in marine muds: Processes, pitfalls, and prospects for paleoflow-speed proxies." *Geochem. Geophy. Geosys.* 7 (10). https://doi.org/10.1029/2006GC001284.
- McNeil, J., C. Taylor, and W. Lick. 1996. "Measurements of erosion of undisturbed bottom sediments with depth." *J. Hydraul. Eng.* 122 (6): 316–324. https://doi.org/10.1061/(ASCE)0733-9429(1996)122:6(316).
- Mehta, A. J. 2013. Vol. 38 of *An introduction to hydraulics of fine sediment transport*. Singapore: World Scientific Publishing Company.
- Mehta, A. J., and W. H. McAnally. 2008. "Fine grained sediment transport." In Sedimentation engineering: Processes, measurements, modeling, and practice, edited by M. Garcia, 253–306. Reston, VA: ASCE.
- Moncure, R., and M. Nichols. 1968. Characteristics of sediments in the James River Estuary, Virginia. Special scientific report (Virginia Institute of Marine Science); No. 53. Gloucester Point, VA: Virginia Institute of Marine Science, College of William and Mary.
- Nichols, M. M. 1972. "Sediments of the James River estuary, Virginia." In Vol. 133 of Environmental framework of coastal plain estuaries, edited by B. W. Nelson, 169–212. Boulder, CO: Geological Society of America.
- Nichols, M. M. 1990. "Sedimentologic fate and cycling of Kepone in an estuarine system: Example from the James River estuary." *Sci. Total Environ.* 97–98: 407–440. https://doi.org/10.1016/0048-9697(90) 90254-R.
- Nichols, M. M., G. H. Johnson, and P. C. Peebles. 1991. "Modern sediments and facies model for a microtidal coastal plain estuary, the James Estuary, Virginia." J. Sediment. Res. 61 (6): 883–899. https://doi.org/10.1306/D42677F8-2B26-11D7-8648000102C1865D.
- Park, K., H. V. Wang, S. C. Kim, and J. H. Oh. 2008. "A model study of the estuarine turbidity maximum along the main channel of the upper Chesapeake Bay." *Estuaries Coasts* 31 (1): 115–133. https://doi.org/10.1007/s12237-007-9013-8.
- Patel, S. J., and B. G. Desai. 2009. "Animal-sediment relationship of the crustaceans and polychaetes in the intertidal zone around Mandvi, Gulf of Kachchh, Western India." J. Geol. Soc. India 74 (2): 233– 259. https://doi.org/10.1007/s12594-009-0125-6.
- Pejrup, M., and O. A. Mikkelsen. 2010. "Factors controlling the field settling velocity of cohesive sediment in estuaries." *Estuarine Coastal Shelf Sci.* 87 (2): 177–185. https://doi.org/10.1016/j.ecss.2009.09.028.
- Perkey, D. W., and S. J. Smith. 2019. *Impact of mud aggregate processes in sediment transport studies*. Rep. No. ERDC/CHL CHETN-VIII-12. Vicksburg, MS: USACE.
- Plint, A. G., J. H. S. Macquaker, and B. L. Varban. 2012. "Bedload transport of mud across a wide, storm-influenced ramp: Cenomanian—Turonian Kaskapau formation, Western Canada foreland basin." J. Sediment. Res. 82 (11): 801–822. https://doi.org/10.2110/jsr.2012.64.
- Rust, B. R., and G. C. Nanson. 1989. "Bedload transport of mud as pedogenic aggregates in modern and ancient rivers." *Sedimentology* 36 (2): 291–306. https://doi.org/10.1111/j.1365-3091.1989.tb00608.x.
- Schaffner, L. C., E. K. Hinchey, T. M. Dellapenna, C. T. Friedrichs, M. Thompson Neubauer, M. E. Smith, and S. A. Kuehl. 2001. "Physical energy regimes, sea-bed dynamics and organism-sediment interactions along an estuarine gradient." In *Organism-sediment interactions*, edited

- by J. Y. Aller, S. A. Woodin, and R. C. Aller, 161–182. Columbia, SC: Univ. of South Carolina Press.
- Schieber, J., J. B. Southard, and A. Schimmelmann. 2010. "Lenticular shale fabrics resulting from intermittent erosion of water-rich muds—interpreting the rock record in the light of recent flume experiments." J. Sediment. Res. 80 (1): 119–128. https://doi.org/10.2110/jsr.2010.005.
- Schiller, L., and A. Naumann. 1933. "Über die grundlegenden berechnungen bei der schwerkraftaufbereitung." Ver. Deut. Ing. 77: 318–320.
- Shen, J., and J. Lin. 2006. "Modeling study of the influences of tide and stratification on age of water in the tidal James River." *Estuarine Coastal Shelf Sci.* 68 (1–2): 101–112. https://doi.org/10.1016/j.ecss.2006.01.014.
- Smith, N. D. 1972. "Flume experiments on the durability of mud clasts."
  J. Sediment. Petrol. 42 (2): 378–383. https://doi.org/10.1306/74D72559-2B21-11D7-8648000102C1865D.
- Smith, S. J., and C. T. Friedrichs. 2011. "Size and settling velocities of cohesive flocs and suspended sediment aggregates in a trailing suction hopper dredge plume." Cont. Shelf Res. 31 (10): S50–S63. https://doi.org/10.1016/j.csr.2010.04.002.
- Soulsby, R. L. 1997. *Dynamics of marine sands: A manual for practical applications*. London: Thomas Telford.
- Soulsby, R. L., and R. Whitehouse. 1997. "Threshold of sediment motion in coastal environments." In *Proc.*, *Pacific Coasts and Ports '97 Conf.*, 149–154. Christchurh, New Zealand: Univ. of Canterbury.
- Taghon, G. L., A. R. M. Nowell, and P. A. Jumars. 1984. "Transport and breakdown of fecal pellets: Biological and sedimentological consequences." *Limnol. Oceanogr.* 29 (1): 64–72. https://doi.org/10.4319/lo .1984.29.1.0064.
- Teifke, R. H., and E. Onuschak. 1973. *Vol. 83 of Geologic studies, coastal plain of Virginia*. Charlottesville, VA: Virginia Division of Mineral Resources.
- Thanh, P. H. X, M. D. Grace, and S. C. James. 2008. Sandia National Laboratories environmental fluid dynamics code: Sediment transport user manual. No. SAND2008-5621. Sandia National Laboratories.

- Thomsen, L., and G. Gust. 2000. "Sediment erosion thresholds and characteristics of resuspended aggregates on the western European continental margin." *Deep Sea Res. Part I Oceanogr* 47 (10): 1881–1897.
- USACE (U.S. Army Corps of Engineers). 2016. The U.S. waterway system: transportation facts & information. Washingon, DC: USACE.
- USACE (U.S. Army Corps of Engineers). 2019. Norfolk District Navigation Data Repository. Washington, DC: USACE.
- USGS (U.S. Geological Survey). 2019. National Water Information System: Web Interface. Reston, VA: USGS. https://waterdata.usgs.gov/nwis/inventory?agency\_code=USGS&site\_no=02037500.
- van Rijn, L. C. 1984. "Sediment transport, part II: Suspended load transport." *J. Hydraul. Eng.* 110 (11): 1613–1641. https://doi.org/10.1061/(ASCE)0733-9429(1984)110:11(1613).
- Warner, J. C., C. R. Sherwood, R. P. Signell, C. K. Harris, and H. G. Arango. 2008. "Development of a three-dimensional, regional, coupled wave, current, and sediment-transport model." Comput. Geosci. 34 (10): 1284–1306. https://doi.org/10.1016/j.cageo.2008.02.012.
- Winterwerp, J. C., W. G. M. van Kesteren, B. van Prooijen, and W. Jacobs. 2012. "A conceptual framework for shear flow-induced erosion of soft cohesive sediment beds." *J. Geophys. Res. Oceans* 117 (C10): C10020. https://doi.org/10.1029/2012JC008072.
- Wright, L. D., L. C. Schaffner, and J. P. Y. Maa. 1997. "Biological mediation of bottom boundary layer processes and sediment suspension in the lower Chesapeake Bay." *Mar. Geol.* 141 (1–4): 27–50. https://doi.org/10.1016/S0025-3227(97)00061-3.
- Wright, V. P., and S. B. Marriott. 2007. "The dangers of taking mud for granted: Lessons from Lower Old Red Sandstone dryland river systems of South Wales." *Sediment. Geol.* 195 (1–2): 91–100. https://doi.org/10.1016/j.sedgeo.2006.03.028.
- Xu, R., and O. A. Di Guida. 2003. "Comparison of sizing small particles using different technologies." *Powder Technol.* 132 (2–3): 145–153. https://doi.org/10.1016/S0032-5910(03)00048-2.